Supporting Information for Generalizable Trends in Electrochemical Protonation Barriers

Anjli M Patel,[†] Sudarshan Vijay,[‡] Georg Kastlunger,[‡] Jens Kehlet Nørskov,[‡] and Karen Chan[*,‡]

[†]*SUNCAT Center for Interface Science and Catalysis, Department of Chemical Engineering, Stanford University, Stanford, CA*

[‡]*Catalysis Theory Center, Department of Physics, Technical University of Denmark, 2800 Kongens, Lyngby, Denmark*

E-mail: kchan@fysik.dtu.dk

SI contents:

Data availability

Atomic structures along the reaction path for all adsorbates and metal surfaces are provided at the following GitHub repository:

`https://github.com/anjlip/protonation_barriers.git`

Additionally, reaction energies and corresponding structures are available in the Catalysis-hub.org database[1] at the following address:

`https://www.catalysis-hub.org/publications/PatelGeneralizable2021`

Energy and charge transfer coefficients along reaction

Figure S1 below displays the potential energy (before and after extrapolation to 0 V_{SHE} along the protonation reaction path) for each metal/adsorbate pair. The corresponding charge transfer coefficients (β) are also shown for the force-based, Bader charge, and DDEC charge estimation methods. Note that the force-based β values are corrected, as described in the **Force method correction** section below. The results reveal several noteworthy trends. Specifically, we observe a shift in the predicted transition state (image with the maximum energy along the reaction path) upon extrapolation of the potential energies to 0 V_{SHE} in many cases.

Given the nature of the constant charge DFT computations used to construct these reaction paths, we also observe an upward shift in the work function (and corresponding potential) within the simulations as the proton is transferred from H_3O^+ to the adsorbate. Note that the work function subsequently slightly decreases after the proton is transferred, which can be attributed to both relaxation of solvent molecules and the hydrogen atom on the adsorbate.

Another noteworthy observation relates to the variation in β along the reaction path across each estimation method. In the case of *C protonation, β (which represents the

potential dependence of a given state) decreases from a positive value to zero from the initial to final state. For the Bader charge method in particular, this is not the case for *N and especially *O protonation. In these cases, β either slightly decreases or remains largely unchanged before the final state, where the value is set to zero. The lack of change in the value of β is in contrast to the change in work function for all of the systems, corresponding to the proton-coupled electron transfer (PCET). The DDEC charge method also shows a decrease in $\Delta\beta$ from *C to *N to *O protonation but to a lesser degree, while the force method does not exhibit this behavior. We examine potential causes for these trends in β values with respect to adsorbate in the following section.

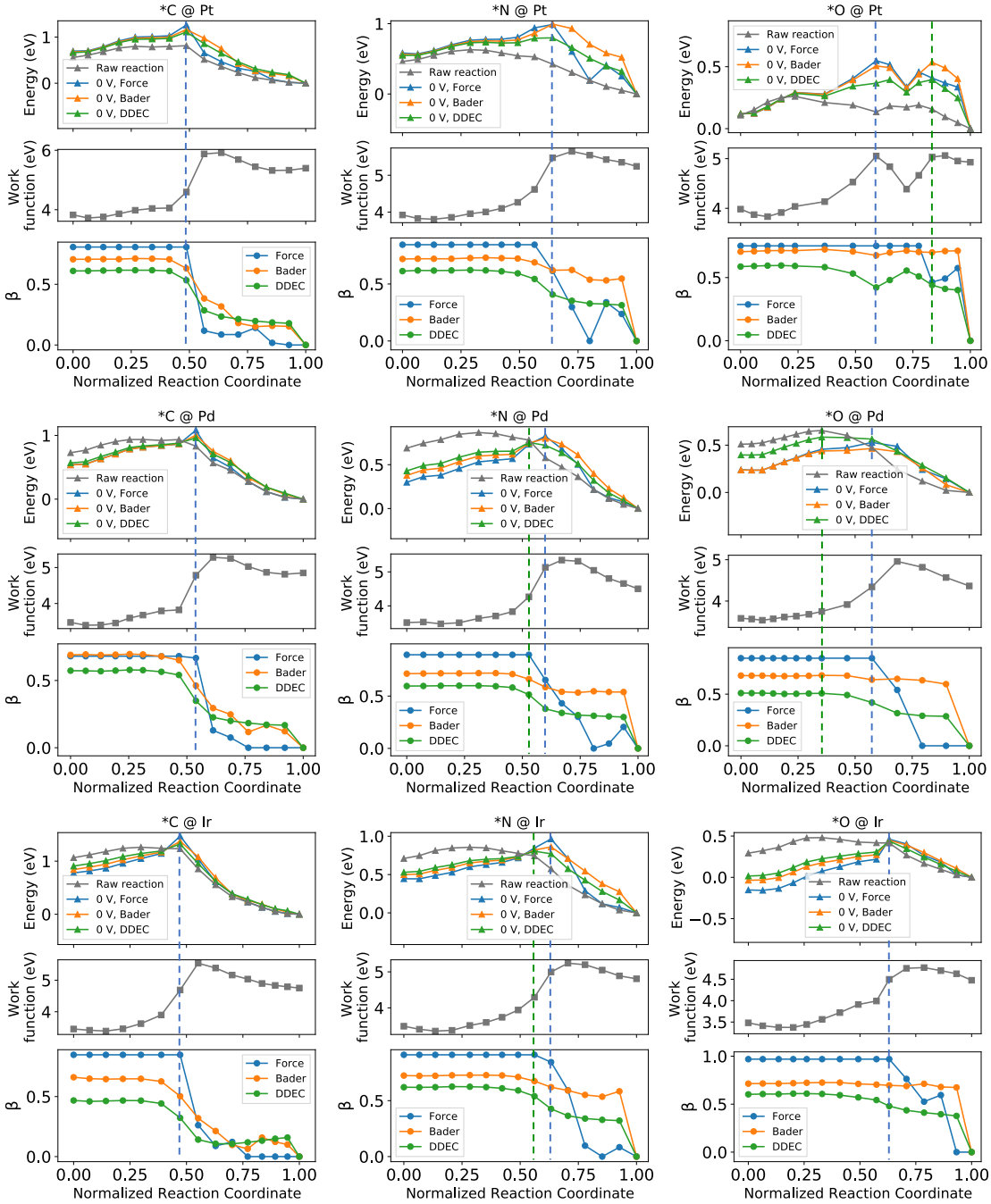

Figure S1: Potential energies (△) and work functions (□) along the reaction path from raw DFT computations (grey) and extrapolated to 0 V_{SHE} for each metal/adsorbate combination. Charge transfer coefficients (β, ○) for each image in the reaction path computed via force method (blue), Bader charge method (orange), and DDEC charge method (green). Dotted lines correspond to 0 V_{SHE} extrapolated transition states for each β computation method.

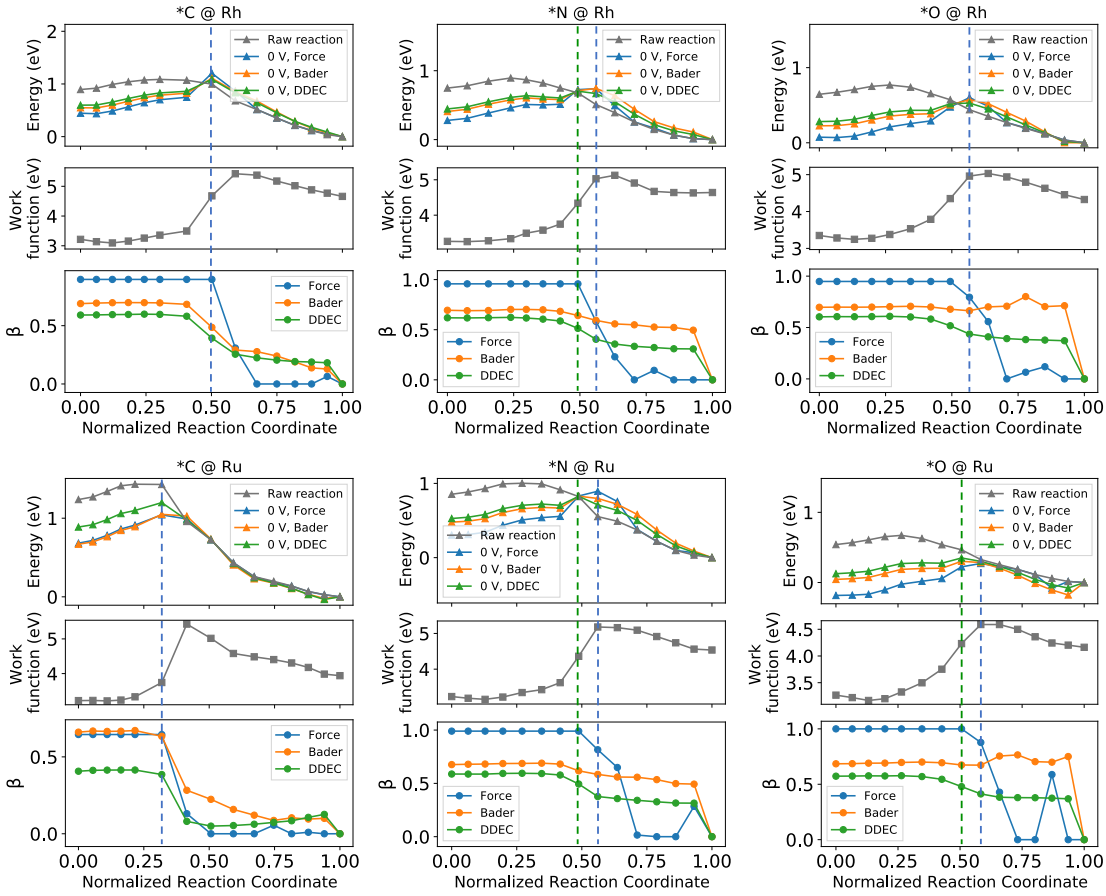

Figure S1: (cont'd) Potential energies (△) and work functions (□) along the reaction path from raw DFT computations (grey) and extrapolated to 0 V_{SHE} for each metal/adsorbate combination. Charge transfer coefficients (β, ○) for each image in the reaction path computed via force method (blue), Bader charge method (orange), and DDEC charge method (green). Dotted lines correspond to 0 V_{SHE} extrapolated transition states for each β computation method.

Charge partitioning methods for β estimation

As shown in Figure S1, the charge partitioning schemes used to determine charge transfer along the protonation reaction path influence the estimated β values. Examining the net charges on various components of the simulated system can provide insight into the observed trends in β across adsorbates and metal surfaces. Figure S2 shows the change in net charge of the adsorbate, proton, metal slab, and water structure from the initial state to the final state

for each metal/adsorbate combination. Both Bader and DDEC charge partitioning schemes are shown. According to Bader partitioning, the proton within the system gains 0.5 e charge when transferred to *C, but its change in net charge is significantly smaller for *N and *O. These qualitative trends are also observed for DDEC partitioning, but to a smaller degree. From the net Bader charges on the adsorbates and metal slabs, a significant portion of the depleted charge from the metal slab during the reaction is allocated to *N and *O adsorbates rather than the transferred proton. This is not the case for *C, which explains the differences in β values for *C protonation versus *N and *O from the Bader charge method. These observations in charge allocation might be explained by the relative electronegativities of *O, *N, and *C adsorbates, where the greater ionic character of the hydrogen-adsorbate bond in electronegative atoms (*O and *N) leads to additional charge allocated to these adsorbates compared to *C after the PCET occurs. While the DDEC method shows qualitatively similar trends in the net charge of the system, the relative differences are generally smaller than those from Bader partitioning. Note that compared to Bader, the DDEC method also shows a positive net charge on the water molecules surrounding the H_3O^+ in the initial state of the reaction. This can be attributed to hybridization of the proton within the water structure in the initial state, resulting in greater distribution of the positive charge. The components of the net charge on each component of the simulated reacting system highlight the limitations of charge-based methods to estimate β.

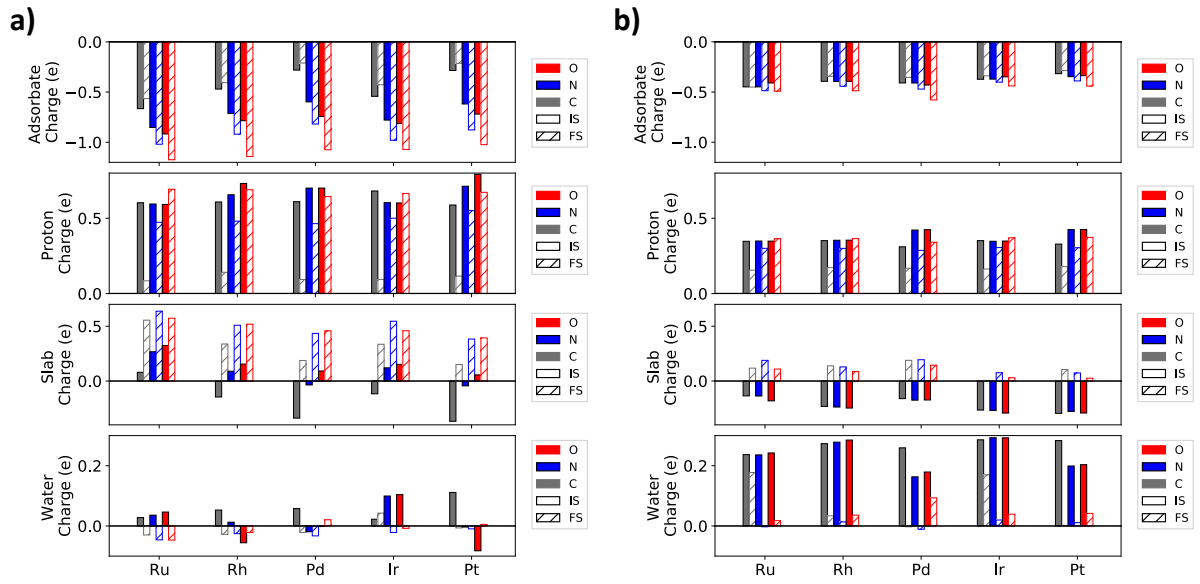

Figure S2: Net a) Bader and b) DDEC charges of adsorbate, proton, metal slab, and water structure in the initial and final states of the adsorbate protonation reactions

The methods used in this work to extract constant potential energetics for electrochemical reactions are based on the assumption that the system can be treated as a parallel plate capacitor. Since the charge of a capacitor varies linearly with its potential, we can test the validity of this assumption by plotting β as a function of potential. Figure S3 shows these plots for β values extracted via the Bader and DDEC charge methods. The results show significant scatter for several metal/adsorbate combinations, suggesting deviations from the ideal capacitor model. However, the DDEC method approaches a linear relationship more closely than Bader in several cases, such as the protonation reactions on Pt and Ir.

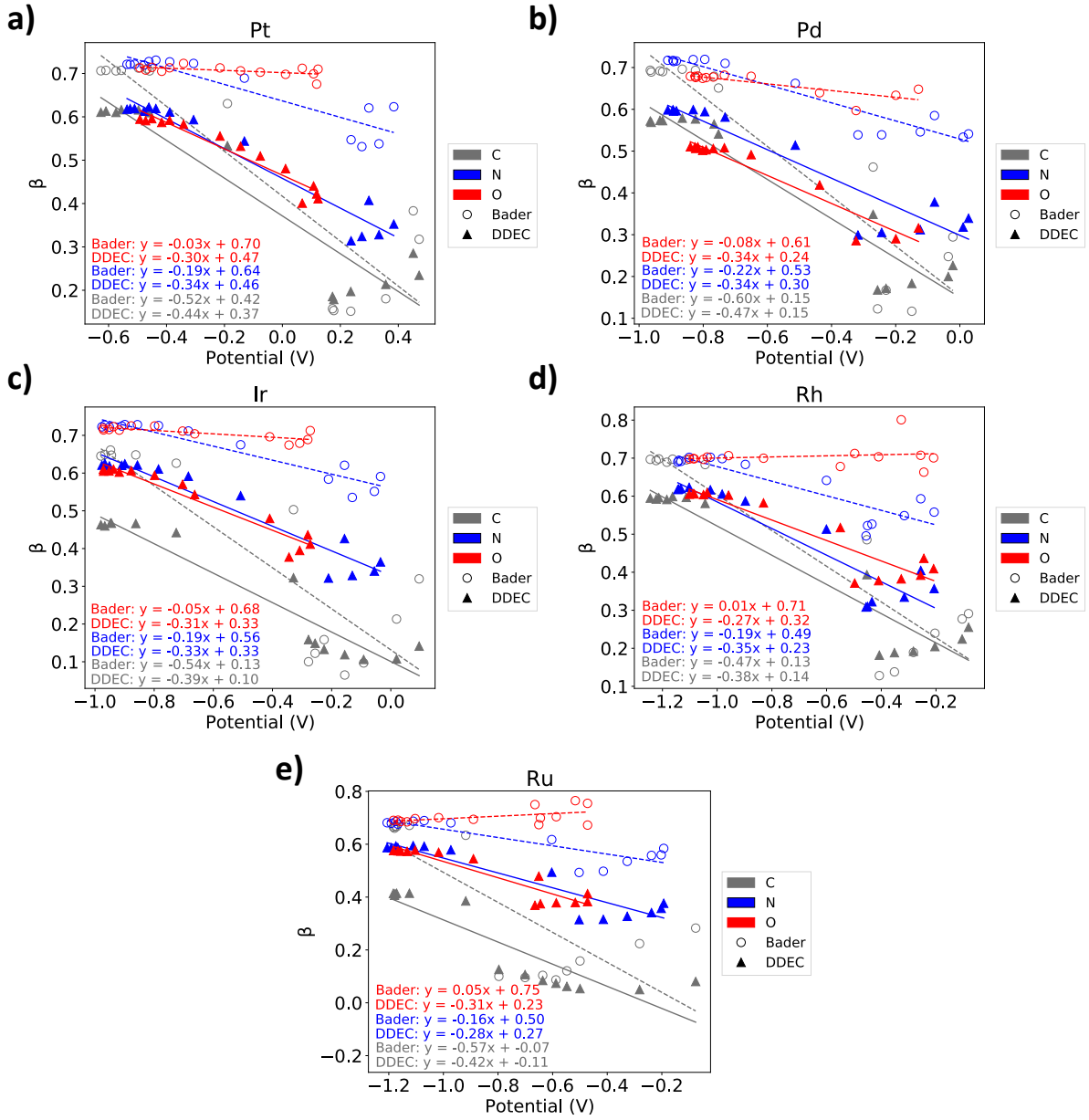

Figure S3: β versus potential for PCET on a) Pt, b) Pd, c) Ir, d) Rh, and e) Ru (111) surfaces.

Figure S4 shows capacitances estimated from linear fits of the plots of β versus potential from Figure S3. We find that most the capacitances from the DDEC method fall within 15 - 25 μF/cm^2. The values from Bader partitioning vary more widely, which can partly be traced to issues with charge partitioning discussed previously.

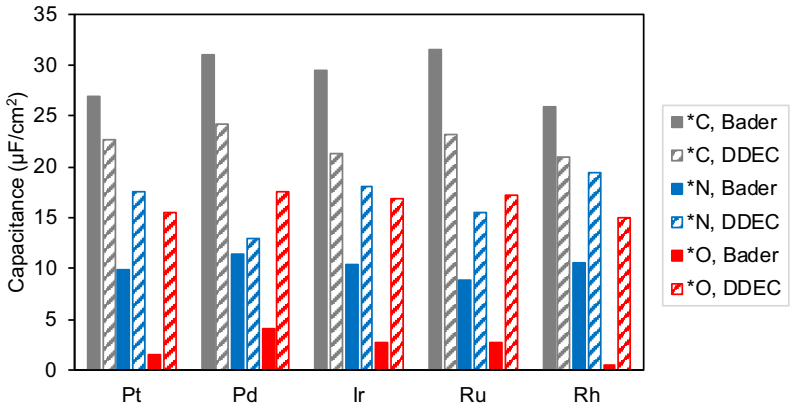

Figure S4: Estimated Capacitances for each metal surface based on trends in β versus work function

Explanation of force method

In light of the challenges associated with charge-based methods to estimate β, an alternative force method developed by Vijay et al was explored. Within this approximation, the electrochemical interface is treated as a capacitor whose charge varies linearly along the reaction path. By performing a first order Taylor expansion of the charge of the capacitor over the normalized reaction coordinate (ω), we arrive at equation S1.

$$q_2 = q_1 + \frac{dq}{d\omega}\Big|_{\omega=0} \cdot \omega \tag{S1}$$

This equation can also be expressed as a function of the dipole moment of the unit cell in the direction normal to the surface ($\frac{d\mu}{dR}$) projected onto ω. $\frac{d\mu}{dR}$ is in turn expressed in terms of the derivative of atom-centered forces within the system with respect to electric field ($\frac{dF}{d\zeta}$) in equation S2.

$$\beta = q_2 - q_1 = \frac{d\mu}{dR}\Big|_{\omega=0} \cdot \omega = \frac{dE}{d|\zeta|dR}\Big|_{\omega=0} \cdot \omega = \frac{dF}{d|\zeta|}\Big|_{\omega=0} \cdot \omega \tag{S2}$$

The value of $\frac{dF}{d\zeta}$ is estimated via a 2-point finite difference grid according to equation S3, where F is the atom-centered force on the transferred proton and 0.1 eV/Åwas used for $\delta\zeta$.

$$\frac{dF}{d|\zeta|} \approx \frac{-F^{j+2} + 8F^{j+1} - 8F^{j-1} + F^{j-2}}{12\delta\zeta} \tag{S3}$$

To evaluate equation S3, the proton within any given image was displaced by 0.01 Å in the direction normal to the surface, and the force on the proton was evaluated from single point DFT calculations at varying applied electric fields (ζ) in the same direction. In addition to evaluating $\frac{dF}{d\zeta}$, it is necessary to define the normalized reaction coordinate (ω). The reaction coordinate is estimated as the unit vector in the direction of the change in position of the proton in a given image to the following image along the reaction path, as shown in equation S4.

$$\omega \approx \frac{r^{i+1} - r^{i}}{||r^{i+1} - r^{i}||} \tag{S4}$$

The charge transfer coefficient is then estimated from $\frac{dF}{d\zeta}$ and ω according to equation S2. Note that the assumptions within this implementation of the force method (linear variation of charge, proton position fully describes the reaction path) can result in significant errors in estimating β far from the transition state. We therefore correct the β values when extrapolating all images along the reaction paths, as described in the **Force method correction** section. By applying the corrected charge transfer coefficients estimated by this method to the capacitor model of the electrochemical interface from equation 2 in the main text, we can extrapolate reaction energetics to constant potential.

Force method correction

The assumptions of the as-implemented force method for estimating β pose challenges for extracting reasonable values far from the true transition state of the system. For instance, the finite difference computation of $\frac{dF}{d\zeta}$ was only performed for the proton transferred within

the system. This can result in errors in estimating the potential dependence close to the initial state in particular, where the proton is hybridized with the H_3O^+ ion and the water structure. In addition, the position-based reaction coordinate between neighboring images introduces errors when sections of the reaction path do not reflect charge transfer (violating the linear change in charge over the course of the reaction). An example of such a case is when a transferred proton rearranges on the *C, *N, or *O adsorbate into a more stable configuration. Figure S5 shows the β values computed directly from the force method for each state along the reaction path of each metal/adsorbate combination. The errors associated with the force method far from the transition state are evident in this figure. For instance, the β values initially increase from 0.2 in the initial state rather than monotonically decreasing, as expected for an electrochemical protonation reaction. In addition, negative β values are observed for certain states due to poorly defined reaction coordinates, especially after the proton is transferred. Since the primary purpose of extrapolating the energetics of the entire reaction path is to identify the true transition state, the error-prone values of β away from the transition state are unlikely to be relevant for our analysis. To avoid identifying an incorrect transition state, we 'correct' the β values by imposing constraints. Specifically, the range of the β values is constrained from 0 to 1. In addition, the value of β from the initial state to the state corresponding to the maximum value of β is set to this maximum value to avoid artificial peaks in the reaction path from an erroneous description of charge transfer far from the transition state. These corrected values of β from the force method are shown in Figure S1.

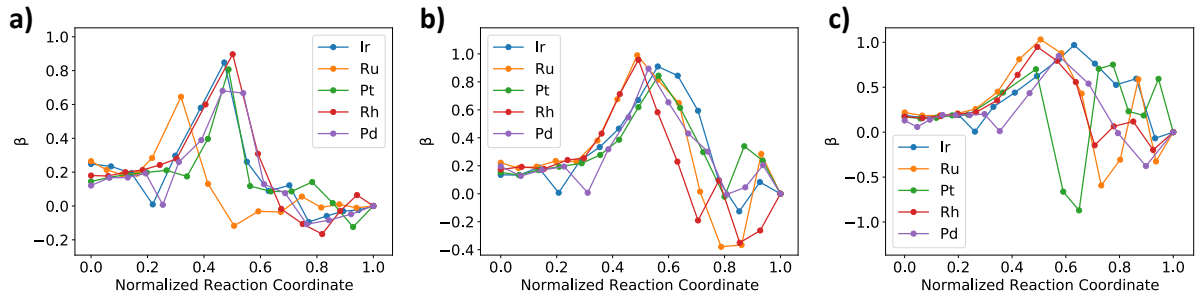

Figure S5: Uncorrected force method β values along reaction path for protonation of a) *C, b) *N, c) *O

Comparison of charge transfer coefficients

Figure S6 displays the value of β at the transition state determined by the Bader charge, DDEC charge, and force methods at 0 V_{SHE} and the intrinsic potential. Despite scatter, particularly at the intrinsic potential, most of the values of β appear to cluster within 0.4 - 0.8.

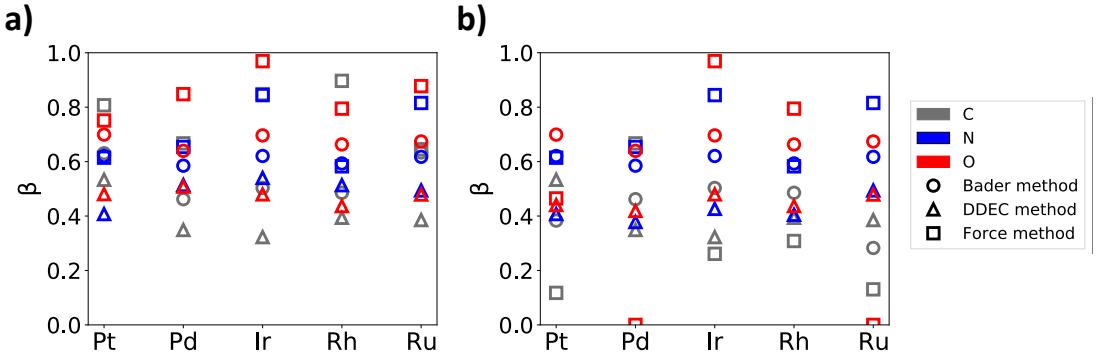

Figure S6: Transition state β values for *C, *N, and *O protonation computed via Bader charge, DDEC charge, and force methods at a) 0 V_{SHE} and b) intrinsic potentials

Protonation barrier sensitivity to charge transfer coefficient method

Figure S7 shows the sensitivity of protonation barriers to the value of β. Barriers computed via the Bader charge, DDEC charge, and force methods are compared to those using a constant β value of 0.6. The results indicate that the scaling trends and barrier groupings are robust with respect to the method used to compute β.

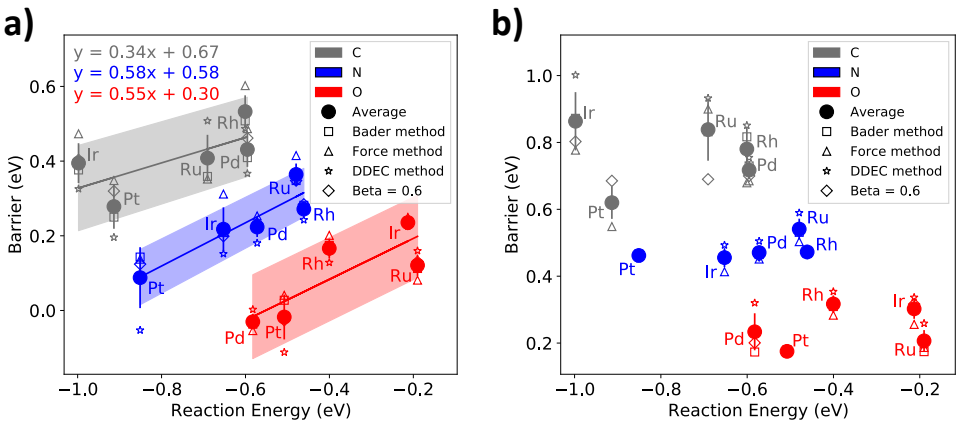

Figure S7: *C, *N, and *O protonation barriers at a) 0 V_{SHE} and b) intrinsic potentials computed using a constant β value of 0.6 and Bader charge, DDEC charge, and force methods of β estimation.

Proton-adsorbate bond order analysis

To understand the origin of protonation barrier groupings by adsorbate, we investigated the change in the DDEC bond order between the transferred proton and *C, *N, and *O adsorbates from the transition state to the final state of the reaction in Figure S8. Figure 5b from the main text indicates that the transition state for *C protonation occurs earlier in the reaction path than that of *N and *O protonation, corresponding to increased transition state barriers. Figure S8 represents the component of the reaction path attributed to the formation of the proton-adsorbate bond. At 0 V_{SHE}, *C shows a significantly larger bond order difference from the transition to final state than the other adsorbates for most of the

surfaces, suggesting that this bond formation may contribute significantly to the adsorbate-based groupings at this potential. However, this trend is not observed at intrinsic potentials. Other factors, such as partial water adsorption to the surface late in the reaction pathway, can also contribute to the observed barrier groupings by adsorbate.

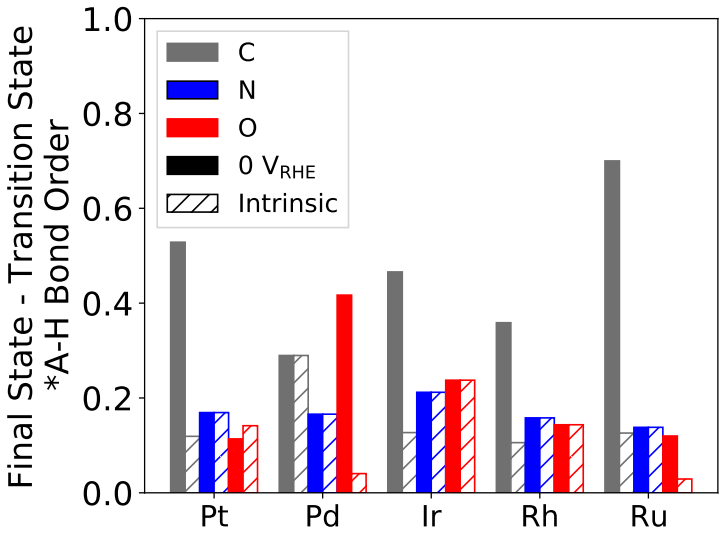

Figure S8: Adsorbate/proton DDEC bond order difference from transition state to final state at 0 V_{SHE} and intrinsic potentials

Water restructuring

Figure S9 visualizes representative changes in the water structure in the final state of the protonation of *C, *N, and *O on Ru(111). We observe greater movement and partial adsorption of water molecules in the case of *C protonation, and this occurs late in the reaction pathway (see full reaction trajectories at `https://github.com/anjlip/protonation_barriers.git`).

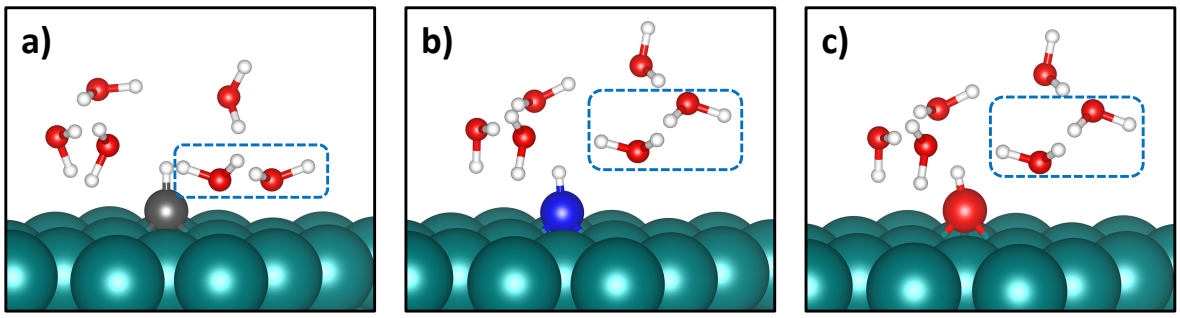

Figure S9: Representative final state structures after PCET to a) *C, b) *N, and c) *O on Ru(111). Dashed boxes highlight water restructuring in the case of *C protonation, which results in stabilization.

Adsorption energy and protonation trends

Based on bond order conservation principles, one might expect a negative correlation between the protonation reaction energy and the adsorption energy of *C, *N, and *O. Specifically, a strong binding metal may 'hog' electrons from the adsorbate to which it is bound, resulting in a relatively weak bond formed with an incoming proton. Figure S10a indeed shows a negative correlation between protonation reaction energy and adsorption energy, but significant scatter is observed for *C in particular. By combining the correlation from Figure S10a with the scaling relationship between protonation barriers at 0 V_{SHE} and reaction energy from Figure 4a, we may estimate these barriers directly from the adsorption energy of a given adsorbate. Figure S10b compares protonation barriers predicted from these scaling relationships (solid line) to a linear fit (dashed line). Despite scatter, the adsorption energy may provide a rough estimate of reaction barriers based on scaling relationships for some metal/adsorbate combinations.

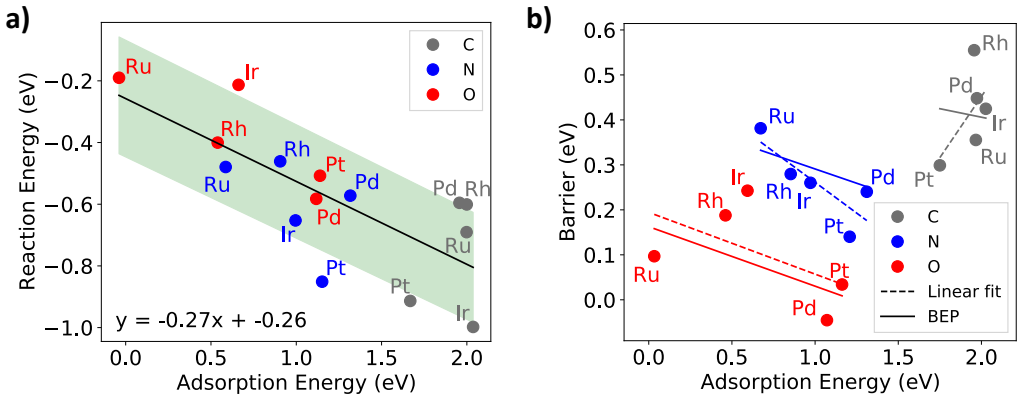

Figure S10: a) Protonation reaction energy versus adsorption energy; b) Protonation barrier at 0 V_{SHE} versus adsorption energy

H-down water structure

As noted in the main text, the water structure used in electrochemical barrier computations can significantly impact the estimated potentials and extrapolated reaction energetics. Previous reports have subtracted the net dipole of the water structure from the computed potentials to counteract this effect.[2–4] To evaluate the generalizability of the observed protonation barrier trends, these reactions were also studied for an alternative explicit water structure shown in Figure S11, referred to as the H-down water structure. For simplicity, we refer to the water structure considered in the main text (Figure 3a) as the H-up water structure. This alternative water structure results in a change in the work function of the system, which in turn affects the computed potential according to the methods described in the main text.

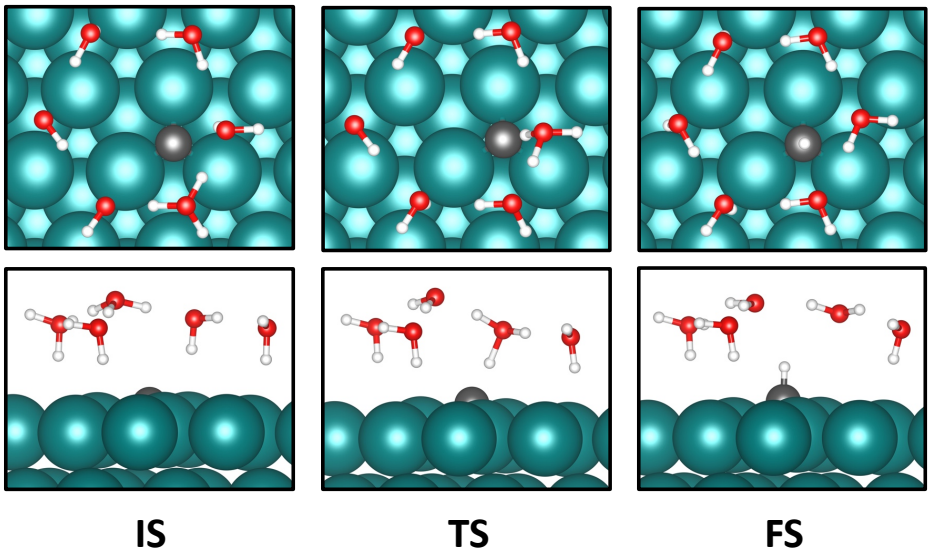

Figure S11: Representative initial, transition, and final states of *C protonation reaction for the H-down water structure

Comparison of H-down charge transfer coefficients

Figure S12 shows the values of β computed via the Bader charge, DDEC charge, and force methods for *C, *N, and *O protonation with the H-down water structure. Compared to the results for the initial water structure in Figure S6, the H-down β values show less scatter but no consistent trend across adsorbates.

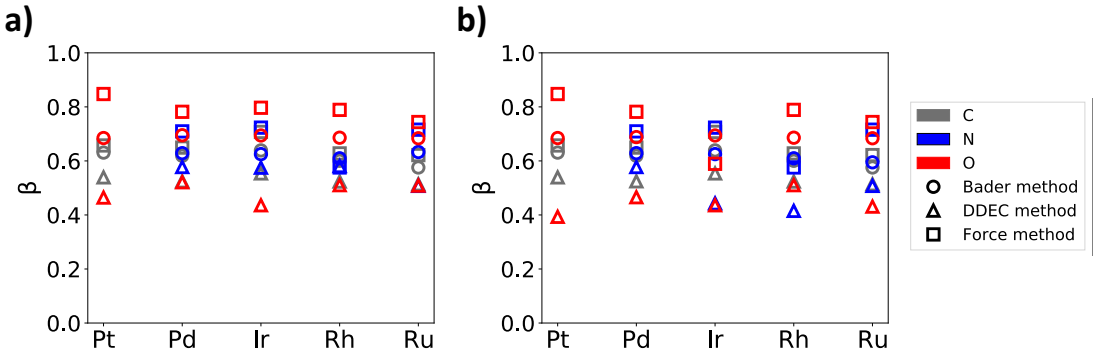

Figure S12: Transition state β values for *C, *N, and *O protonation for the H-down water structure computed via Bader charge, DDEC charge, and force methods at a) 0 V_{SHE} and b) intrinsic potentials

H-down protonation barrier trends

Figure S13 shows the *C, *N, and *O protonation barriers for the H-down water structure computed at 0 V_{SHE} and intrinsic potentials using the Bader charge and force methods to estimate β. Compared to the H-up water structure (studied in the main text, Figure 3a), the H-down structures result in overall larger barriers, which is largely an artifact of the difference in work function from these calculations. There is also a greater spread in the computed barriers for each metal/adsorbate combination depending on the method used for extrapolation. This increased range can be traced to larger potentials associated with the H-down water structure, resulting in greater differences in the computed barriers upon extrapolation to 0 V_{SHE} and intrinsic potentials. Despite the increased scatter, similar groupings arise in the 0 V_{SHE} and intrinsic barriers for the protonation reactions, where the adsorbates exhibit the following order of increasing barriers: *O < *N < *C.

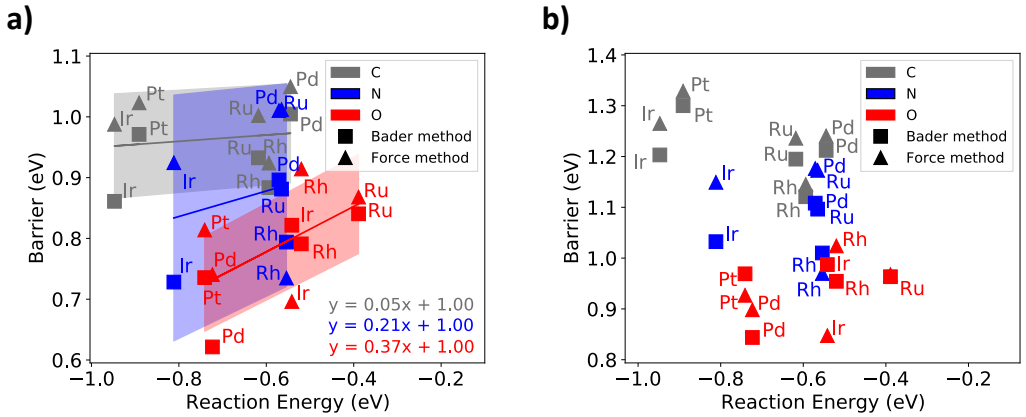

Figure S13: *C, *N, and *O protonation barriers for H-down water barrier trends at a) 0 V_{SHE} and b) intrinsic potentials.

Water structure stability

Given the two sets of protonation barriers for the H-up and H-down water structures, it is useful to evaluate their relative stability to determine the most relevant set of data. Figure S14 shows the difference in potential energy of the final state for *C, *N, and *O protonation in the H-down water structure minus that in the H-up water structure. While the stability of varying water structures is potential-dependent, we consider the H-up water structure in the main text based on its relative stability compared to the H-down structure in the final state of the reaction and the proximity of the computed mean potentials for PCET in the H-up structure to our targeted 0 V_{SHE} potential in this report.[5]

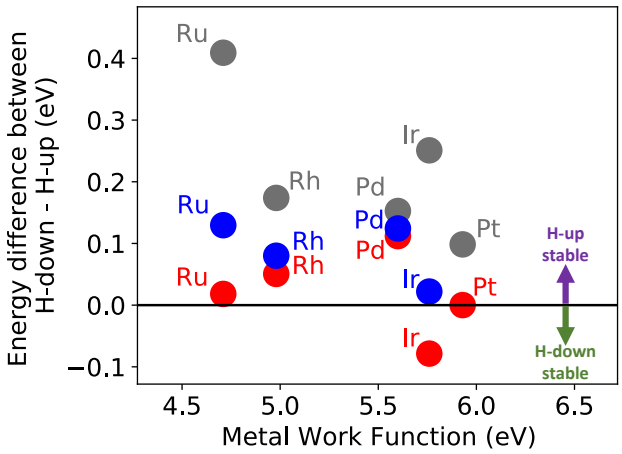

Figure S14: Energy difference of H-down minus H-up final state for *C, *N, and *O protonation

Charge Extrapolation Example

The following example demonstrates charge extrapolation for *C protonation on Pt(111) with the H-up water structure to 0 V_{SHE}. The protonation reaction barrier is computed by first extrapolating the reverse (oxidation) barrier and determining the forward reaction barrier relative to the CHE reference state for the bulk proton. Note that within Equations S5 and S6, the energy values (E) used to compute potential energy differences ($\Delta E_{reverse}$ and $\Delta E_{a0,reverse}$) are raw electronic energies from DFT computations performed according to the methods described in the main text.

$$\Delta E_{forward} = E_{*CH} - E_{*C} - \frac{1}{2}E_{H_2} = -163.87\text{ eV} - (-159.39\text{ eV}) - \frac{1}{2}(-7.15\text{ eV}) = -0.91\text{ eV} \tag{S5}$$

$$\Delta E_{a0,reverse} = E_{*C-H} - E_{*CH} = -163.06\text{ eV} - (-163.87\text{ eV}) = 0.81\text{ eV} \tag{S6}$$

$$\overline{\Phi} = \frac{\Phi_{*\mathrm{C-H}} + \Phi_{*\mathrm{CH}}}{2} - 4.44\ \mathrm{eV} = \frac{4.59\ \mathrm{eV} + 5.39\ \mathrm{eV}}{2} - 4.44\ \mathrm{eV} = 0.54\ \mathrm{eV} \tag{S7}$$

$$\beta = q_{*\mathrm{C-H}} - q_{*\mathrm{CH}} = 0.58 - (-0.05) = 0.63 \tag{S8}$$

$$\Delta E_{a,\mathrm{reverse}} = \Delta E_{a0,\mathrm{reverse}} + \beta * \overline{\Phi} = 0.81\ \mathrm{eV} + (0.63) * (0.54\ \mathrm{eV}) = 1.13\ \mathrm{eV} \tag{S9}$$

$$\Delta E_{a,\mathrm{forward}} = \Delta E_{a,\mathrm{reverse}} + \Delta E_{\mathrm{reverse}} = 1.13\ \mathrm{eV} - 0.91\ \mathrm{eV} = 0.25\ \mathrm{eV} \tag{S10}$$

Tabulated Extrapolated Barrier Data

Table S1 shows the overall reaction energies and barriers for each of the protonation reactions considered in Figure 4 in the main text.

Table S1: Reaction Energies and Barriers of PCET to *C, *N, and *O on Metal Surfaces with H-up Water Structure

Adsorbate	Metal	Reaction Energy (eV)	Barrier at 0 V_{SHE} (eV)		Barrier at Intrinsic Potential (eV)	
			Bader	Force	Bader	Force
C	Pt	-0.91	0.25	0.35	0.62	0.55
C	Pd	-0.60	0.41	0.49	0.73	0.69
C	Ir	-1.00	0.38	0.47	0.87	0.78
C	Rh	-0.60	0.51	0.60	0.82	0.68
C	Ru	-0.69	0.36	0.35	0.83	0.90
N	Pt	-0.85	0.14	0.14	0.47	0.47
N	Pd	-0.57	0.23	0.25	0.46	0.45
N	Ir	-0.65	0.21	0.31	0.46	0.41
N	Rh	-0.46	0.28	0.28	0.47	0.47
N	Ru	-0.48	0.35	0.41	0.53	0.50
O	Pt	-0.51	0.03	0.04	0.18	0.17
O	Pd	-0.58	-0.04	-0.05	0.17	0.24
O	Ir	-0.21	0.24	0.25	0.30	0.26
O	Rh	-0.40	0.17	0.20	0.31	0.28
O	Ru	-0.19	0.11	0.08	0.17	0.19

Barrier Trend Statistics

Table S2 shows the linear (BEP) fit equations, root mean squre errors (RMSE), and regression coefficients (r^2) for the protonation reaction barriers at 0 V_{SHE} versus the overall reaction energy with the H-up water structure (corresponding to the trends in Figure 4 in the main text).

Table S2: Linear Fits and Statistics for 0 V_{SHE} Protonation Barriers versus Reaction Energy for each Adsorbate with H-up Water Structure

Adsorbate	**BEP Fit**	**RMSE (eV)**	**Regression Coefficient (r^2)**
C	y = 0.28x + 0.63	0.07	0.30
N	y = 0.47x + 0.54	0.04	0.73
O	y = 0.49x + 0.29	0.07	0.54

Protonation Barriers on Cu(111)

Cu-based catalysts are particularly relevant to electrochemical processes like CO_2 reduction, which is a prime example of a complex reaction network that can benefit from simplifying PCET barrier trends. However, the significantly smaller lattice constant of Cu(111) compared to the other metal surfaces studied in this work render protonation barrier computations with consistent water structures difficult in this case. Table S3 shows *C, *N, and *O protonation reaction energies and barriers computed using the same methods described in the main text on Cu(111). The hexagonal water structure used in these calculations is consistent across these three reactions, but it is unique from the H-up and H-down structures considered for the other metals studied herein. While this makes it difficult to directly compare these barriers to those of the materials, we do observe that the relative orderings of the protonation reaction energies (*O > *N > *C) and barriers (*C > *N > *O) are consistent with the trends reported in the manuscript. These results provide further evidence of the generalizability of these trends.

Table S3: Reaction Energies and Barriers of PCET to *C, *N, and *O on Cu(111)

Reaction	ΔE (eV)	Barrier (ΔE_a) at 0 V_{SHE} (eV)	Barrier (ΔE_a) at Intrinsic Potential (eV)
$^*C + (H^+ + e^-) \longrightarrow {}^*CH$	-1.01	1.67	1.83
$^*N + (H^+ + e^-) \longrightarrow {}^*NH$	-0.93	1.31	1.56
$^*O + (H^+ + e^-) \longrightarrow {}^*OH$	-0.43	1.28	1.35

Convergence Tests for System Size

Due to the increased computational demand of transition state searches via the NEB method, the metal slabs simulated in this work were limited to 3x3 metal slabs with three layers of atoms. Of these three layers of atoms in the metal surface, the positions of the bottom two layers were fixed at bulk lattice constants. To test the convergence of these calculations, the reaction energies of PCET reactions were compared between the 3-layer slab model and a 4-layer model again containing two layers of fixed atoms. Table S4 shows the sensitivity of the raw reaction energies of the three PCET reactions studied in this work on Rh(111) and Ir(111) surfaces to the number of layers in the metal slab.

Table S4: Raw Reaction Energies of Protonation Reactions for 3-layer and 4-layer Slabs

Reaction	Surface	ΔE, 3 layers (eV)	ΔE, 4 layers (eV)
*C + (H+ + e-) ⟶ *CH	Rh(111)	-0.89	-0.88
	Ir(111)	-1.07	-0.99
*N + (H+ + e-) ⟶ *NH	Rh(111)	-0.75	-0.71
	Ir(111)	-0.71	-0.64
*O + (H+ + e-) ⟶ *OH	Rh(111)	-0.65	-0.44
	Ir(111)	-0.29	-0.16

References

(1) Winther, K. T.; Hoffmann, M. J.; Boes, J. R.; Mamun, O.; Bajdich, M.; Bligaard, T. Catalysis-Hub.org, An Open Electronic Structure Database for Surface Reactions. *Scientific Data* **2019**, *6*, 75.

(2) Shi, C.; Hansen, H. A.; Lausche, A. C.; Nørskov, J. K. Trends in Electrochemical CO2 Reduction Activity for Open and Close-Packed Metal Surfaces. *Physical Chemistry Chemical Physics* **2014**, *16*, 4720.

(3) Liu, X.; Xiao, J.; Peng, H.; Hong, X.; Chan, K.; Nørskov, J. K. Understanding Trends in Electrochemical Carbon Dioxide Reduction Rates. *Nature Communications* **2017**, *8*, 15438.

(4) Tang, M. T.; Liu, X.; Ji, Y.; Norskov, J. K.; Chan, K. Modeling Hydrogen Evolution Reaction Kinetics through Explicit Water–Metal Interfaces. *The Journal of Physical Chemistry C* **2020**, *124*, 28083–28092.

(5) Karlberg, G. S.; Rossmeisl, J.; Nørskov, J. K. Estimations of Electric Field Effects on the Oxygen Reduction Reaction Based on the Density Functional Theory. *Physical Chemistry Chemical Physics* **2007**, *9*, 5158.